



Article

From Material to Solution: Implementing Shape Memory Behavior of Thermoplastic Polymers in Commercial FEA Software for Structural Analysis

Fabian Neumann ¹,*• , Ferdinand Cerbe ² and Michael Sinapius ²

- ¹ German Aerospace Center (DLR), Institute of Lightweight Systems, 38108 Braunschweig, Germany
- Institute of Mechanics and Adaptronics, Technical University of Braunschweig, 38106 Braunschweig, Germany; f.cerbe@tu-braunschweig.de (F.C.); m.sinapius@tu-braunschweig.de (M.S.)
- * Correspondence: fabian.neumann@dlr.de

Abstract: The production of one-piece composite hollow profiles with undercuts presents significant challenges to conventional mold concepts. Mandrels made of thermoplastic shape-memory polymers could facilitate demolding and reduce tooling costs. To design molds in a commercial environment, it is critical to determine their behavior using off-theshelf Finite Element Analysis (FEA) software. This paper investigates all of the necessary steps, from the material model generation, its implementation in commercial FEA software, to the simulation of shape-memory test specimens under unidirectional tensile loading with off-the-shelf FEA modules. The material investigated is PA6. Differential Scanning Calorimetry (DSC) is used to determine the glass transition, crystallization and melting temperatures of the material. The Dynamic Mechanical Analysis (DMA) is then used to determine the elastic modulus versus temperature and frequency. A viscoelastic material model is derived from DMA data. Parameters necessary for the implementation are derived by using fully open-source Python scripts. A unidirectional shape-memory tensile test simulation is performed and compared with the experimental data from a thermo-mechanical shape-memory test. The applied methods allow for the generation and implementation of a viscoelastic material model in commercial FEA software. The simulation shows good results in comparison with the thermo-mechanical shape-memory test. In conclusion, the straightforward "from material to solution" path presented allows us to model and simulate the shape memory behavior of viscoelastic polymers.

Keywords: shape memory polymer (SMP); finite element analysis (FEA); dynamic mechanical analysis (DMA); viscoelasticity



Academic Editor: Alborz Shokrani

Received: 26 January 2025 Revised: 17 February 2025 Accepted: 20 February 2025 Published: 25 February 2025

Citation: Neumann, F.; Cerbe, F.; Sinapius, M. From Material to Solution: Implementing Shape Memory Behavior of Thermoplastic Polymers in Commercial FEA Software for Structural Analysis. J. Manuf. Mater. Process. 2025, 9, 73. https://doi.org/10.3390/ jmmp9030073

Copyright: © 2025 by the authors. Licensee MDPI, Basel, Switzerland. This article is an open access article distributed under the terms and conditions of the Creative Commons Attribution (CC BY) license (https://creativecommons.org/licenses/by/4.0/).

1. Introduction

Fiber-reinforced polymer (FRP) composites have become a leading material in aerospace applications due to their excellent fatigue resistance, superior material properties, and the ability to customize performance by adjusting fiber angles. Today, FRP accounts for approximately 50% of the structural mass in modern commercial aircraft, such as the Airbus A350 and Boeing 787. In sectors such as general aviation and unmanned aerial vehicles (UAVs), FRP accounts for more than 90% of the structural mass [1]. In addition, the market for urban air mobility is expected to grow significantly, with projections of 160,000 passenger drones in use by 2050, although some uncertainties remain regarding the certification and performance of these aircraft [2,3]. Demand for FRP parts is also expected to increase over the next decade in the production of pressure vessels for hydrogen-powered

vehicles, including cars and aircraft [4]. Highly automated manufacturing processes will be essential to meet this growing demand. However, producing complex hollow profiles, with smooth internal surfaces and undercuts, such as struts, air intake ducts, and Type V pressure vessels, remains challenging for traditional tool-based manufacturing methods. Suitable techniques for the automated production of these components include filament or towpreg winding, automated fiber placement (AFP), and braiding [5]. Not considering lost cores of plaster, wax, or similar materials, research into the use of removable mandrels for the automated production of hollow composite profiles began in the late 1990s. Lehmann et al. [6] investigated bladder molding and flow dynamics within the resin transfer molding (RTM) process. Inflatable cores, such as silicone or film bladders, are easily removed from undercuts, but are not suitable for preforming. Removable and reusable cores, that can serve as mandrels in automated manufacturing processes for hollow composite profiles with undercuts, must remain rigid during preforming at room temperature, but must be demoldable after curing. This requires a mechanism that can either change the shape of the mandrel, or adjust its material properties to allow for easy removal from undercuts. Polymers, particularly those experiencing the temperature shape memory effect, have potential for such applications [7]. These polymers are referred to here as shape memory polymers (SMPs). The SMPs could facilitate the production of one-piece, all-composite pressure vessels (Type V), such as those used in hydrogen-powered vehicles, without the need for soluble cores. For example, a pressure vessel could be wound onto a polymer mandrel, which could be easily removed after curing. In addition, S-shaped air intake ducts could be produced using automated fiber placement (AFP) without the need for costly multi-piece rigid tooling. As examined in the previous study by Neumann, research on thermoplastic shape memory polymers for tooling application is very limited [7]. In addition, no literature could be found on the shape memory effect of blow-molded articles. However, neat thermoplastic polymers are widely used in 4D printing. Fourdimensional printing is the 3D printing of stimuli-responsive polymers in which internal stresses, material orientations, or multi-material configurations are introduced during the printing process. This can be understood as a shape programming step. Subsequently, shape recovery is activated in an according manner. The recent literature on this topic has focused primarily on polylactic acid (PLA) and acrylonitrile-butadiene-styrene (ABS), with a much smaller proportion investigating the 4D printing properties of polycarbonate (PC), polyamide-6 (PA6), polyethylene terephthalate-glycol (PETG), thermoplastic polyurethane (TPU), polypropylene (PP), polyether ether ketone (PEEK), and polyvinyl alcohol (PVA). ABS exhibits high impact resistance and good mechanical properties, but degrades under UV light. PLA is biodegradable and easy to print, with a high dimensional accuracy, but has a very low heat resistance. PC has a high thermal and mechanical strength, but its high viscosity makes it difficult to print. PA6 has a high toughness, flexibility and impact resistance, but also has a relatively high moisture absorption. PETG shows good mechanical properties, with better flexibility than PLA, but has a lower heat resistance than ABS. TPU has a high elasticity and abrasion resistance, but is difficult to print. PP has an excellent chemical and impact resistance, but high shrinkage and warpage. PEEK has an excellent chemical resistance and high mechanical properties, but this expensive material requires very high processing temperatures. PVA is water soluble and absorbs moisture, leading to degradation [8]. However, out of the 3D printing materials mentioned, only PA6 and PP are widely used in blow molding, the technology to which this research contributes.

1.1. Classification of Shape Memory Polymers

Shape memory polymers can be categorized in several ways, including by the general type of polymer, the base polymer, or the activation method [9]. The major types

of SMPs are: (1) partially cured thermosets, (2) fully cured thermoset systems, and (3) thermoplastics [10]. In addition, some SMPs have been developed as blends of these main types [11]. However, each category has its drawbacks. Partially cured thermosets continue to cure during their use as SMPs, resulting in changes in the material properties with each cycle. Thermoplastic SMPs tend to creep, i.e., they gradually lose their shape memory over time [10]. As a result, most research has focused on fully cured thermoset systems. Morphological characteristics allow for the classification of SMPs into four distinct types: chemically cross-linked amorphous polymers, chemically cross-linked semi-crystalline polymers, physically cross-linked amorphous polymers, and physically cross-linked semi-crystalline polymers [12]. Based on the base polymer, extensive research on polyamide-based SMPs [13,14], polyurethane-based SMPs [15,16], styrene-based SMPs [17,18], epoxy-based SMPs [19,20], and cyanate-ester-based SMPs [21,22] can be found in the literature. The activation mode for the shape memory effect varies. The temperature-induced shape memory effect (SME) is the most common [7,23], but the effect can also be current-induced [24], light-induced [25], microwave-induced [26], magnetic induced [27], or water-/solution-induced [28]. Research on the tooling applications of SMPs has focused primarily on unreinforced thermoset materials, particularly those based on styrene. Thermoplastic polymers are less commonly used, and the addition of reinforcements limits the allowable strain in the temporary shape. The ability to change shape in these studies is based on either a shape memory effect or a softening process, both of which are triggered by heating in all cases studied in the review by Neumann [7]. Miadowitz [29] introduced thermoplastic blow-molded mandrels to produce hollow composite profiles without a shape memory effect. Blow-molded mandrels also allow production rates to be decoupled from the number of mandrels available, as the blow-molding technology allows multiple positive mandrels to be rapidly produced from a single negative mold. In addition, complex curved struts and tubes, such as those used in trusses or fluid lines, can be efficiently produced either on blow-molded mandrels or by using SMP mandrels tailored to the specific shape of each part. Neumann et al. [30] investigated the suitability of other thermoplastic polymers for use as mandrel materials in the manufacture of composite hollow profiles.

1.2. Contitutive Models of SMPs

Theoretical constitutive models have been developed to understand the shape memory mechanism and to optimize SMPs. Three established methods for constitutive models can be found in the literature: (1) rheological models, (2) phase transition models, and (3) unit cell based multi-branch models. In addition, there are new model building methods in the literature that replace the fitting parameters with physics-based parameters, combine different SMP models, or incorporate multiple algorithms and functions [12].

1.2.1. Rheological Models

The first models used for SMPs were phenomenological visco-elastic and visco-elastic plastic models. These models have three main elements representing the behavior of polymer chains at the macroscopic level: (1) elastic springs, (2) viscous dashpots, and (3) slip elements. Tobushi et al. [31] were the first to introduce a four-element model, with a sliding element representing strain storage and release. The underlying mechanism of this model is that an unrecoverable creep strain occurs when the creep strain exceeds a certain threshold and the temperature falls below the glass transition temperature (T_g), causing the molecular chains to freeze and increase internal friction. Early rheological models have limitations in accurately predicting the shape memory effect; however, they may be sufficient for an initial or rough prediction. Later, researchers introduced modifications, including nonlinear terms

and three-dimensional frameworks, to improve their accuracy [12,32]. A significant advance by Diani et al. [33] was the use of a generalized Maxwell or Maxwell-Wiechert model (GMM), which recognizes that relaxation occurs over a distribution of times rather than at a single time, and the Williams-Landel-Ferry (WLF) equation to describe the relationship between relaxation time and temperature. Since rheological models are relatively easy to solve, this model, along with the WLF equation and Simo's finite strain extension [34] of the generalized Maxwell model, is available in commercial finite element analysis (FEA) software such as ABAQUS 2024 or ANSYS 2023R2, facilitating the integration of viscoelastic behavior in simulations [35]. The GMM is shown in Figure 1. Despite improvements, rheological models often include numerous parameters, without considering the heating rate and the strain rate. Furthermore, they are only capable of describing one-dimensional SME. These characteristics make it possible to use rheological models to describe SMPs for both free and constrained stress recovery tests, with acceptable accuracy.

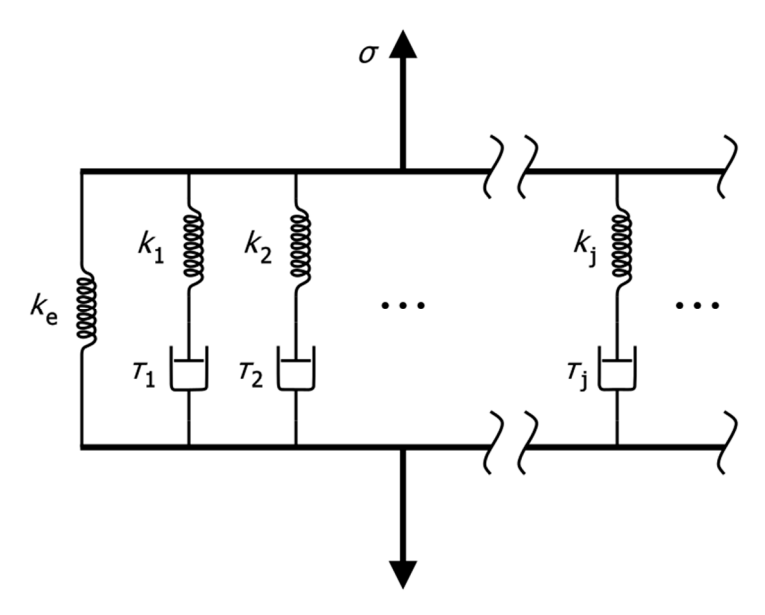


Figure 1. Generalized Maxwell or Maxwell-Wiechert model for viscoelastic materials with spring constants k_e , $k_1 \dots k_j$ and damping constants $\tau_1 \dots \tau_j$ and under tension σ .

1.2.2. Phase Transition Models

The phase transition model was introduced by Liu et al. in 2006 to overcome the limitations of rheological models [36]. Further developments of this approach were contributed by Chen and Lagoudas [37], Wang et al. [38], Baghani et al. [39], and Li et al. [40]. The phase transition model considers SMPs as composites consisting of two distinct phases: (1) an active phase and (2) a frozen phase. The active phase has a high chain mobility and its deformation is primarily entropic, while the frozen phase has a low chain mobility and its deformation is primarily energetic. Shape memory occurs because the proportions of active and frozen phases vary with temperature. When an SMP is cooled below its T_g , the active phase transitions to the frozen phase. This transition traps the deformed state of the material. When the SMP is reheated above its T_g , the frozen phase transitions back to the active phase, returning the material to its original, undeformed shape. Advantages of this constitutive model include the ability to model the three-dimensional shape memory behavior with only six fitted material parameters. Accurate determination of the volume fractions of the active and frozen phases at different temperatures is critical for phase transition models. However, this determination is often based on empirical formulas or fitting experimental data, which may not have a clear physical meaning and may vary depending on the model and material chosen. While the model is clear and understandable for semi-crystalline polymers, it is only a conceptual simplification for amorphous polymers. This limits the physical interpretation of the model. As a rheological model, the phase transition model does not consider the heating rate or strain rate [33]. In addition, it can only model small deformations. Beyond these limitations, the model is capable of describing the SME for constrained stress recovery and free strain recovery with better accuracy [12,32].

1.2.3. Multi-Branch Models

Qi et al. introduced a new multi-branch model in 2008 [41]. This model is based on a representative unit cell of the SMP network and combines the rheological model and the storage strain-based phase transition model. This way, it is possible to achieve more advantages than with the other two models. A key strength is its ability to link the macroscopic deformation observed at the bulk level with the microscopic deformation occurring at the molecular level. This is achieved by integrating the Arruda-Boyce model, which describes the behavior of polymer chains within a representative unit cell. This model assumes that the molecular chains are distributed along the diagonals of a square unit cell in principal strain space. This integration allows the model to better capture nonlinear deformation behavior. In addition, Qi et al. introduced a flow rule to describe plastic softening, allowing the model to describe strain rate effects. Finally, the introduction of a hyperelastic spring element allows for a better representation of the elastic behavior of the material. However, a major drawback of this model is that many parameters must be determined by curve fitting. This makes the model complex to implement [12].

1.3. Implementation in FEA Software

Finite element analysis has been an established method for simulating the shape memory behavior of SMP since the development of the constitutive models mentioned above. However, most of the published work is based on "user-defined mechanical material behavior" (UMAT) subroutines for ABAQUS. Writing these subroutines is time-consuming and requires FORTRAN programming skills. Fortunately, the GMM and the WLF equation, as well as the finite strain extension of the GMM for large deformations, as published by Simo [34], are already implemented in the standard material modules of ABAQUS and ANSYS. In this way, viscoelastic shape memory behavior can be easily implemented via modulus and relaxation time pairs of the Prony series and WLF parameters. This procedure was established by Diani et al. [33], Yu et al. [42], and Azzawi et al. [35]. In particular, the procedure described by Azzawi et al. is still widely used in the recent literature [43,44]. However, all of the available literature relies on proprietary software, such as NLREG or TA Advantage, to calculate the WLF and Prony series parameters. This software is not open source, and licenses must be purchased to use it. Open source software offers significant advantages over proprietary software and contributes to more accessible and transparent research results. It allows users to inspect, modify and verify the code, building transparency and trust. The code can be adapted or used in other software projects to meet the specific needs of future work. Because it is free to use, open source software is cost-effective and gives users full control over their software environment by not locking them into specific vendor ecosystems or licensing models. This, in turn, contributes to a wider compatibility and interoperability of the software with other software projects.

This paper follows the procedures established by Diani et al. and Azzawi et al., but relies on fully open source Python 3.12.9 scripts for parameter identification to allow for a fully transparent and traceable procedure [45].

1.4. Aim of This Work

There is no study in the literature that spans from material coupon tests, through their evaluation, to the implementation of the material model in FEA software for SMP, using fully open-source and transparent methods. Therefore, the purpose of this work is to serve as a guideline for the aforementioned steps in order to achieve a time-efficient and cost-effective finite element simulation of the shape memory behavior. Since the overall goal of the authors' research group is to develop a high-rate manufacturing method for composite hollow profiles on blow-molded mandrels, this study focuses on thermoplastic polymers. Therefore, PA6 is investigated in this study. However, the methods used in this work are easily transferable to other types of polymers. Furthermore, all methods used should be easily accessible and usable with off-the-shelf commercial FEA software to allow an easy transfer from research to commercial mandrel design. The basic material parameters are investigated by DSC and DMA as described in Sections 2.2 and 2.3. Then, a rheological model is used for their implementation. Therefore, the viscoelasticity is represented by a generalized Maxwell model. To calculate the necessary parameters for the Prony series, complex shear and elastic modulus are measured via Rheometry, as described in Section 2.4. Since for thermorheologically simple materials the influence of temperature on the material behavior is the same as that of time, a time-temperature superposition is developed, as described in Section 2.5. WLF shift function parameters are calculated, as described in Section 2.6, and used for the implementation in the FEA software. Section 2.7 introduces a shape memory test procedure to validate the simulation solutions. Section 3 shows the results obtained using the aforementioned methods. The results are discussed in Section 4 and a conclusion is drawn in Section 5.

2. Materials and Methods

This chapter describes the materials used and methods required to determine the necessary parameters for implementing shape memory behavior in off-the-shelf FEA software, such as ABAQUS 2024 or ANSYS 2023R2. The equipment is listed in Table 1. First, a DSC is performed to determine boundary conditions and parameters for the DMA and shape memory testing. Second, the DMA test specimens are fabricated by injection molding. Third, a DMA is performed to investigate the relationship between temperature and Young's modulus. It should be noted that this step is not necessarily required, but helps to define the temperature range and maintain safe operation, within the limits of the equipment for the subsequent complex shear and tensile modulus measurements. Fourth, the complex shear and tensile modulus are determined using frequency and temperature sweeps. As a final step, a shape memory tensile test is performed to validate the simulation results. The schematic workflow is shown in Figure 2.

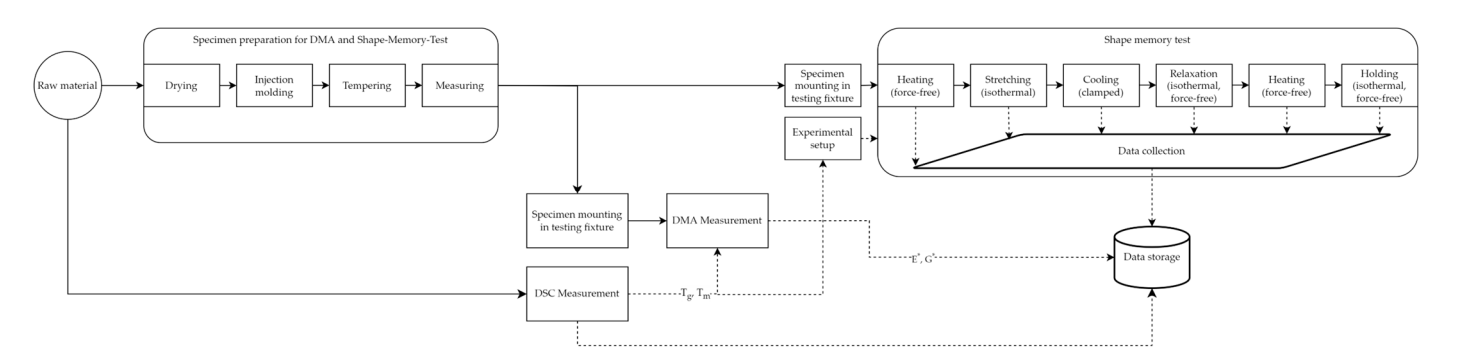


Figure 2. A schematic representation of the experiments.

Table 1. Methods and ed	quipment used	for thermoanalysis.
-------------------------	---------------	---------------------

Method	Equipment	Parameters
Specimen preparation	HAAKE™ MiniJet Pro (Thermo Fisher Scientific Inc., Waltham, MA, USA)	Cylinder: 250 °C Mold: 30 °C Pressure: 300 bar
DSC	DSC 2 TOPEM (Mettler Toledo Inc., Columbus, OH, USA)	25 °C 260 °C; 10 K/min
DMA Shape-Memory-Test	MCR 702 (Anton Paar Group AG, Graz, Austria) MCR 702 (Anton Paar Group AG, Graz, Austria)	25 °C 75 °C; 0.1 Hz 10 Hz 80 °C 20 °C 80 °C; 4.3% strain

2.1. Polymers

Previous work has shown that PA6 and PET are suitable as mandrel material for composite hollow profile production [30]. While PA6 can be processed by extrusion blow molding (EBM), PET is mainly used for injection stretch blow molding (ISBM). ISBM requires an additional preform step, while EBM blows an extruded preform directly into the mold. This makes it much easier to scale in size, which is a key consideration for larger applications. Therefore, PA6 (Durethan BC550Z 900116; Envalior GmbH, Düsseldorf, Germany) is chosen for further investigation in this study. Durethan BC550Z is an unreinforced PA6 designed to meet the demands of extrusion blow molding. It is heat stabilized and has an improved impact resistance. It is widely used for pressure vessels and tank systems. The material comes as granules. The granules are fed into the mini injection molding machine Thermo Scientific HAAKE MiniJet Pro to produce the DMA test specimen (60 mm \times 10 mm \times 1 mm). The physical and mechanical properties of the material used are shown in Table 2.

Table 2. Physical and mechanical properties of PA6 (Durethan BC550Z) [46].

Property	Value	Unit
Elastic modulus	2000	MPa
Yield stress	50	MPa
Yield strain	4.0	%
Tensile strain at break	140	%
Poisson ratio	0.4	
Melting temperature	219	°C
Heat deflection temperature	53	°C
Coefficient of thermal expansion	1.4	$10^{-4}/{ m K}$
Density	1070	kg/m^3
Water absorption	9.1	%
Drying temperature	80	°C
Drying time	2–6	h

2.2. Measurement of Characteristic Temperatures via DSC

In order to determine the boundary conditions and parameters for the DMA and shape memory testing, it is critical to first examine the material by DSC. The most important properties are the glass transition temperature $T_{\rm g}$, crystallization temperature $T_{\rm c}$, and melting temperature $T_{\rm m}$. The glass transition temperature is used to define the temperature range for DMA and shape memory tests. Additionally, it serves as the reference temperature for the master curve construction described in Section 2.5. The effect of crystallization is neglected in this simulation approach because the WLF equation does not cover the molecular changes, see Section 2.6. Therefore, the temperature of shape memory tests and their simulation must stay below the crystallization onset temperature. Staying below the melting temperature is an obvious constraint for all further tests described below. The

measurement is performed with a Mettler DSC 2 TOPEM. Four samples are tested. All results agree well with the manufacturer's melting temperature. Based on the material data sheet, the temperature range over which the sample is heated and cooled is set to 25–260 °C. The heating and cooling rate is set to 10 K/min. No isothermal holds are used. Two heating cycles and one cooling cycle are performed. The first heating cycle is used to erase the previous thermal history of the material. This includes any previous thermal treatments, such as processing or storage conditions. By heating the sample above its melting temperature, the molecular structure is reset, allowing a more accurate evaluation of its properties. The results of the DSC measurement of the used PA6 are shown in Section 3.1.

2.3. Measurement of Complex Shear and Young's Modulus via DMA

The Complex Shear and Young's Modulus are determined via DMA, using an Anton Paar Modular Compact Rheometer (MCR) 702, with an additional linear drive and a solid rectangular fixture (SRF) for the specimen. Due to space limitations in the test chamber, one injection molded sample is cut in half to obtain two samples. Both samples were tested and showed similar results. For ease of direct data processing, the test data from one specimen measuring 32.156 mm \times 10.03 mm \times 1.07 mm is used for further data processing. The test is performed for frequencies between 0.1 and 10 Hz and for discrete temperatures between 25 °C and 75 °C, with 5 °C steps. The DMA is performed to investigate the relationship between temperature and moduli, with regard to the frequency to apply time-temperature superposition as described in Section 2.4. The rheometer and test specimen are shown in Figure 3.



Figure 3. Rheometer Anton Paar MCR 702 with test specimen.

2.4. Master Curve

Various experimental methods, such as DMA [33] or relaxation experiments [42], can be used to construct a master curve for a viscoelastic material. DMA is an efficient method for identifying the properties within the linear viscoelastic region of the material [47]. This type of experiment requires testing at multiple frequencies and temperatures. The tensile storage modulus is measured over a frequency range of 0.1 to 10 Hz and a temperature range of 25 °C to 75 °C, using the Rheometer Anton Paar MCR 702 in the DMA mode. By applying the time–temperature superposition (TTS) principle, these storage moduli are adjusted in the frequency domain, allowing for the development of the master curve. In this process, the fitted frequency is the experimental frequency multiplied by a shift factor a, as expressed in Equation (1). Typically, the shift factor a is expressed in logarithmic form (e.g., a = 10 is expressed as log10(a) = 1). The relationship between the shifted frequency f shift and the experimental frequency f is defined in Equation (1) as follows:

$$f_{\text{shift}} = f \cdot a \tag{1}$$

where f and a represent the frequency and the shift factor, respectively. To create a continuous curve that approximates the behavior of the material, $f_{\rm shift}$ must be determined by aligning the data points. Constructing the master curve involves manual fitting of the data or using optimization methods, as published by Lennon et al. [48]. The developed algorithm is also published as an open source Github repository under the GPL-3.0 license and is available as a pip installation (pip install mastercurves) for direct implementation in custom software projects [49]. We used this routine to implement the mastercurves 0.2.3 into our code and to generate the master curve from our measurement data, which showed good results, as described in Section 3.3. The reference temperature $T_{\rm ref}$ was set to 50 °C. The TTS principle is expressed by Equation (2) for the storage and loss modulus:

$$E'(f,T) = E'(f_{\text{shift}}, T_{\text{ref}})$$

$$E''(f,T) = E''(f_{\text{shift}}, T_{\text{ref}})$$
(2)

The TTS generates shift factors a(T) that allow frequency adjustments to match other experimental temperatures. For simulations, interpolation between experimental temperatures is required, and the shift factors can be approximated using the WLF equation. The following section details the fitting of the WLF equation to these shift factors.

2.5. William-Landel-Ferry Regression

The Williams-Landel-Ferry equation approximates the shift factors to describe the temperature-dependent relaxation behavior in polymers. This approach, along with alternatives such as the Arrhenius equation, relies on selecting parameters that best match the experimental shift factors a from the TTS. The WLF equation is particularly effective when the reference temperature $T_{\rm ref}$ is the glass transition temperature of the polymer, and the constants C_1 and C_2 are tailored to the specific polymer [50].

Typically, the WLF equation is expressed in terms of the logarithm of the shift factor, as shown in Equation (3):

$$\log(a) = \frac{-C_1(T - T_{\text{ref}})}{C_2 + (T - T_{\text{ref}})}$$
(3)

Data measured at temperatures below $T_{\rm ref}$ result in a positive $\log(a)$, shifting to higher frequencies, characterizing the short-term behavior of the material in colder conditions. Conversely, data above $T_{\rm ref}$ result in a negative $\log(a)$ that shifts to lower frequencies, representing the long-term behavior of the material. This behavior implies that polymers relax faster at temperatures above $T_{\rm ref}$ and slower at temperatures below $T_{\rm ref}$, which is well

in line with the typical behavior of thermoplastic polymers. Williams et al. [50] emphasize that the WLF equation is most accurate for amorphous polymers above their glass transition temperature. This means explicitly that the equation does not account for two effects:

- Crystallization at the crystallization temperature T_c : Neglecting crystallization can lead to an underestimation of the long-term modulus as the material crystallizes, since crystallization increases the long-term modulus. Therefore, to accurately simulate SMPs, it is important to stay below the onset of crystallization as determined by DSC experiments.
- Limit for relaxation times below T_g :
 Omitting this aspect leads to an overestimation of the relaxation times τ_k , suggesting that the material would relax and creep faster under experimental conditions.

To calculate the WLF parameters, the shift factors derived from the master curve constitution are read into a Python data frame. Equation (3) is defined as a function of its parameters. A curve fit is performed using the *Scipy* function *curve_fit*. Finally, the calculated WLF parameters are saved and a plot of the WLF equation and shift factors is drawn for verification. The initial parameters are chosen in accordance with Williams et al. $(C_1 = 8.86, C_2 = 101.6)$ [50]. The reference temperature is set to 50 °C, in accordance with the DMA results described in Section 3.2.

2.6. Prony Series Parameter Determination

The Prony series represents the viscoelastic behavior of materials in a way that parallels the relaxation characteristics of a GMM (see Figure 1). The relaxation modulus equation follows a similar form, as shown in Equation (4). As mentioned above, the Prony series parameters can be obtained from various test methods, including stress relaxation tests, creep tests, or DMA. The relaxation modulus E(t) is represented as a sum of terms that describe the long-term modulus E_{∞} and a series of exponential decay components. Each term in the series is characterized by a modulus E_k and a relaxation time τ_k , where k indicates each element in the series:

$$E(t) = E_{\infty} + \sum_{k=1}^{n} E_k e^{-t/\tau_k}$$
 (4)

Unlike Equation (4), DMA data represent the viscoelastic response in the frequency domain. The link between the time and frequency domains is provided by the Fourier transformation, and applying the Fourier transformation to Equation (4) results in Equation (5), with ω being the angular frequency [47].

$$E^*(\omega) = E_{\infty} + \sum_{k=1}^n E_k \frac{\omega^2 \tau_k^2}{1 + \omega^2 \tau_k^2} + i \sum_{k=1}^n E_k \frac{\omega \tau_k}{1 + \omega^2 \tau_k^2}$$
 (5)

The real part of the complex modulus $\Re(E^*)$ is called the storage modulus $E'(\omega)$, and the imaginary part $\Im(E^*)$ is called the loss modulus $E''(\omega)$. This leads to Equations (6) and (7).

$$E'(\omega) = E_{\infty} + \sum_{k=1}^{n} E_k \frac{\omega^2 \tau_k^2}{1 + \omega^2 \tau_k^2}$$
 (6)

$$E'(\omega) = E_{\infty} + \sum_{k=1}^{n} E_{k} \frac{\omega^{2} \tau_{k}^{2}}{1 + \omega^{2} \tau_{k}^{2}}$$
 (7)

The parameter fitting is performed using the curve_fit function from the Scipy 1.14.1 Python package. The script Prony_FrequencyDomain.py reads the frequencies as well as storage and loss modulus from the master curve and optimizes E_{∞} as well as a defined

number of E_k and τ_k pairs. In this study, the Prony parameters are fitted only to the storage modulus data and not to the loss modulus data. While technically possible, we have observed convergence problems with the Python curve_fit function when fitting parameters to both parts of the complex modulus equation at the same time. The derived parameters are then implemented into the loss modulus equation. While this allows for a more accurate fit of the storage modulus data, it may result in a less accurate fit for the loss modulus. Because the loss modulus accounts for energy dissipation and relaxation behavior during recovery, an underestimate results in a less viscous drag. This results in a faster predicted recovery and the simulation fails to reproduce the gradual energy dissipation observed in the experimental data. Overestimation can have the opposite effect.

2.7. Rheometer Shape-Memory Test

A shape memory test is performed to verify the simulation based on the material model derived from the Prony series curve fitting. The test is performed with an Anton Paar MCR 702 rheometer with a linear drive, as shown in Figure 3. Two samples of PA6 Durethan 550BC with a nominal size of 10 mm \times 2 mm \times 1 mm (measured: 10.39 mm \times 2.2 mm \times 1.07 mm; 10.91 mm \times 2.4 mm \times 1.10 mm) are used. Possible errors in the shape-memory test are as follows: instrumental errors, such as sample, clamp, or fixture misalignment; sample preparation errors, such as inconsistent geometry or defects and internal stresses; environmental errors, such as humidity or temperature variations; operational errors, such as incorrect frequencies or strain amplitudes. The specimens are produced with precision-milled injection molds and measured multiple times with calibrated measuring tools. The specimens are dried and annealed to relieve internal stresses and eliminate moisture. The controlled environment of the test laboratory minimizes the environmental errors. The shape-memory test setup is developed iteratively. This eliminates potential errors step by step and ensures a valid test procedure. The test is performed in a calibrated, high-precision Anton Paar MCR 702 rheometer, which allows for highly reproducible tests based on the same test specification. Finally, two samples are tested and evaluated based on the iteratively developed test specification. The derived results allow for a qualitative statement, but do not represent a large statistical distribution. The samples are mounted in the SRF of the rheometer. The starting condition for the test procedure is defined as no load on the specimen and a temperature of 80 °C. The test sequence is defined in five steps: (1) stretching the specimen to 4.3% strain at a constant temperature (80 $^{\circ}$ C); (2) Cooling the specimen to 20 °C at constant strain (4.3%); (3) releasing the force to 0N at constant temperature (20 $^{\circ}$ C); (4) heating the specimen to 80 $^{\circ}$ C at constant force (0N); (5) holding the specimen at constant temperature (80 °C) and at constant force (0N). Since the first two steps are position-controlled, while steps four and five are force-controlled, it is necessary to ensure a safe transition between these modes. Therefore, step three is introduced. Step three is a position-controlled transition step where the elastic strain is released under a defined linear motion until a force condition (0.01 N) is met. The tensile force of $0.01~\mathrm{N}$ is maintained to ensure correct data collection by the rheometer. Figure 4shows a schematic illustration of the shape memory test procedure with the three control variables: temperature (T), force (F), and strain (e).

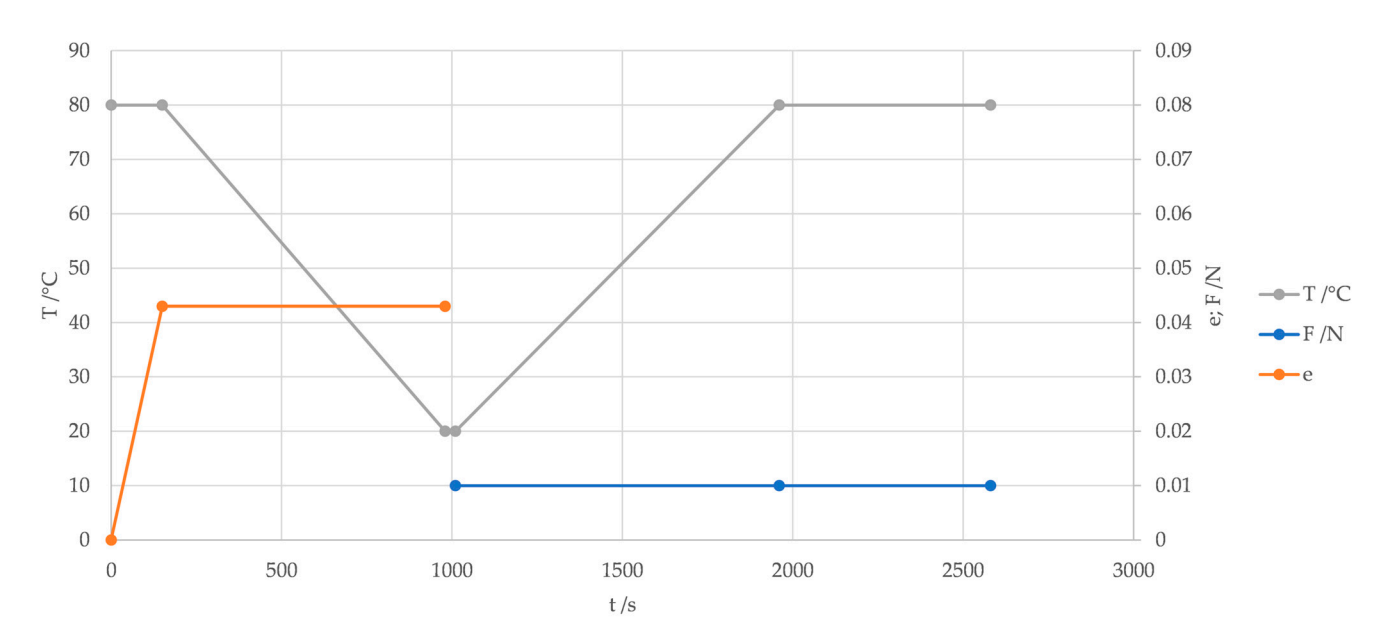


Figure 4. Schematic illustration of the shape memory test procedure with the process parameters temperature (T), force (F), and strain (e) over time (t).

3. Results

All measurements are carried out in the thermo-analytical laboratory of the DLR—Institute of Lightweight Systems in Braunschweig, Germany. The results of the previously introduced methods are presented in the subsequent subchapters. Furthermore, the implementation in ANSYS Mechanical is described in Section 3.4.

3.1. Results of the DSC

The DSC of the PA6 shows standard thermal properties for this type of semi-crystalline polymer, including characteristic $T_{\rm g}$ and $T_{\rm m}$ values and a moderate level of crystallinity, consistent with the typical properties. Figure 5 shows the graph of the measurement. In the first cycle, the glass transition onset is observed at 44.15 °C and an endpoint at 74.01 °C. No clear ISO midpoint could be found. In the second cycle, the onset is observed at 48.49 °C, the ISO midpoint at 55.82 °C, and the endpoint at 75.88 °C. This shift between cycles suggests possible relaxation effects or slight reorganization of the polymer chains as the material heats up. Since the PA6 is hygroscopic, the absorbed water also affects the values measured during the first heating cycle. This is typical behavior and the reason for carrying out two thermal cycles. Therefore, only the data measured after the first heating will be examined further. The melting peak in the second cycle is 222.51 C. During the cooling phase, a reverse peak at 181.36 °C marks the crystallization process. The degree of crystallinity calculated from the enthalpy values provides crystallinity values of 19.38% and 18.64%. This is within the expected range for PA6. The results of the DSC are summarized in Table 3.

Table 3. Summarized results of the DSC.

Measurand	Mean Value	Standard Deviation
T_{g}	54.23 °C	1.45 °C
T_{m}^{o}	222.17 °C	0.43 °C
$T_{\mathbf{c}}$	182.52 °C	2.05 °C
Crystallinity	20.07%	1.10%

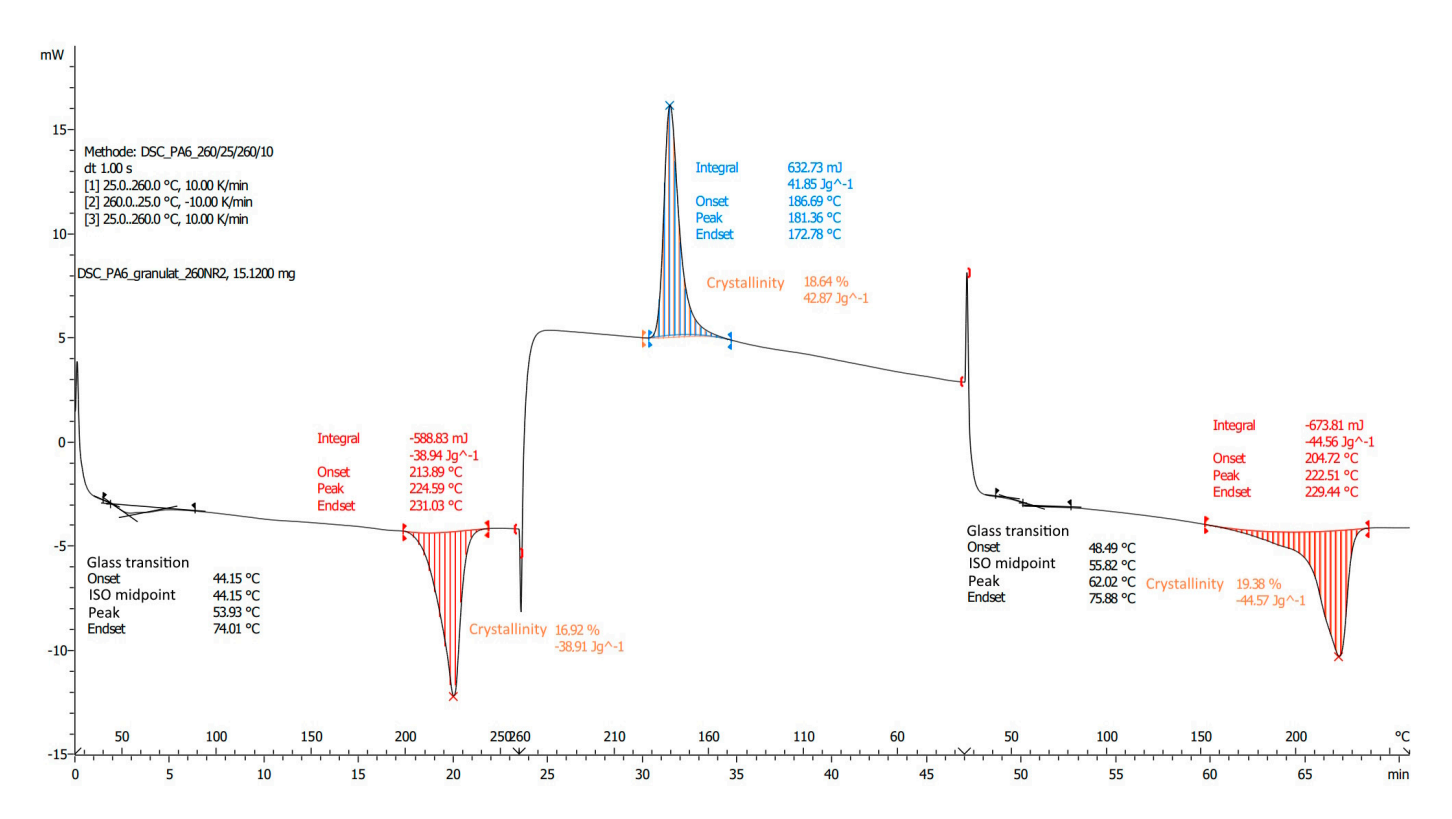


Figure 5. Results of the DSC measurement of PA6.

3.2. Results of Complex Tensile and Shear Modulus Test via DMA

Complex tensile and shear modulus are measured using the Anton Paar MCR 702 rheometer with linear drive as described in Section 2.3. Figure 6 shows the results for tensile storage and loss modulus, as these values are further used to apply TTS and evaluate the Prony parameters. The storage modulus is above the loss modulus in the temperature range. This means that the material behaves more elastic than viscos, which is also referred to as a viscoelastic solid. This is the expected behavior in this temperature range. The storage modulus represents the elastic behavior of the material, and the energy stored during deformation. At lower temperatures of up to 40 °C, the storage modulus is at about 1800 MPa. In this temperature range, the material is in its glassy state. From 40 $^{\circ}$ C to 70 $^{\circ}$ C the storage modulus decreases to about 300 MPa. This reflects the reduction in elasticity of the material across the glass transition. Above 70 °C the glass transition is complete, and the material is in its rubbery state. The loss modulus measures the viscous behavior of the material and represents the energy dissipation during deformation. At temperatures below 30 °C, the loss modulus is at approximately 100 MPa, indicating low energy dissipation and elastic material behavior. Between 40 °C and 50 °C the loss modulus shows a peak, indicating glass transition and high energy dissipation. Above 60 °C, the loss modulus drops below 100 MPa, as the material softens further.

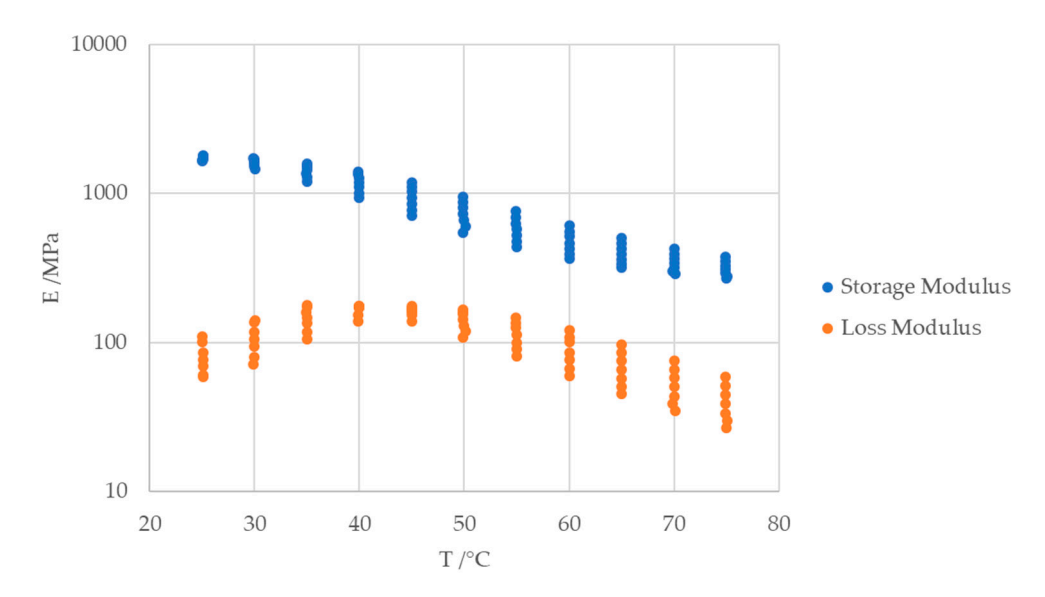


Figure 6. Complex tensile modulus depending on temperature from DMA measurements.

3.3. Parameter Identification

The parameter identification for the Prony series and the WLF equation is performed according to the method described in Sections 2.5–2.7. First, the complex modulus data derived by DMA is shifted to a master curve using the TTS principle with the Mastercurve.py v1 Python script. The DMA data are shown in Figure 7a. The storage modulus is plotted against frequency at temperatures ranging from 25 °C to 75 °C. As discussed in Section 3.2, higher temperatures correspond to lower storage modulus. Figure 7a also shows that lower frequencies correspond to lower storage moduli, while higher frequencies correspond to higher storage moduli. At low frequencies, the material has more time to respond to deformation. Viscoelastic relaxation results in lower stiffness or elastic modulus. At high frequencies, the sample undergoes deformation in a short time. Therefore, the material has less time to relax, resulting in stiffer material behavior. This effect is also measurable at higher temperatures, where the material softens and allows for higher molecular mobility. In this way we observe a frequency dependent stiffening effect. Running the Mastercurve.py v1 script on these data results in Figure 7b. Data from the temperatures above the reference temperature are shifted left, to the lower frequencies, while data from lower temperatures are shifted right, to the higher frequencies. The result is a smooth master curve with no outliers. The narrow confidence interval band in Figure 7a and the resulting smooth master curve indicate a high quality of the input data and a good applicability of the time-temperature superposition principle. It also indicates a well-defined glass transition behavior. At low frequencies, between 10×10^{-3} and 10×10^{-1} Hz, the storage modulus is low, indicating the rubbery state of our material. Between 10×10^{-1} and 10 Hz Young's modulus increases sharply, indicating the glassy transition zone, where the material changes from a viscous to an elastic state. At higher frequencies, the material behaves as a stiff elastic solid. The calculated shift parameters a are shown in Table 4.

Table 4. Shift factors *a* for the tested frequencies.

T/°C	25	30	35	40	45	50	55	60	65	70	75
$\log_{10}(a)$	5.270	4.145	2.965	1.879	0.889	0	-0.828	-1.596	-2.304	-2.910	-3.456

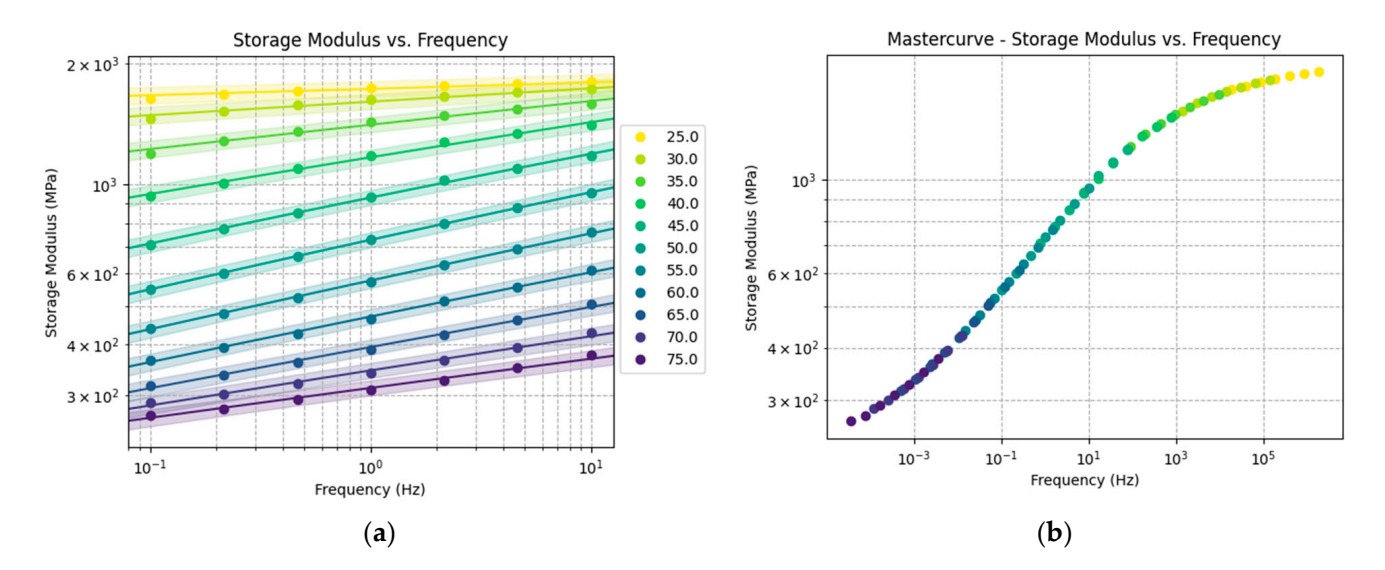


Figure 7. Storage Modulus vs. Frequency: (a) frequency sweeps at different temperatures (25...75 °C); (b) master curve derived from (a) by Python script.

The shift parameters for each frequency sweep at the discrete temperatures are then used to calculate a curve fit for Equation (3) and determine the WLF parameters. To do this, the curve_fit function from the Scipy 1.14.1 Python package is used in the published WLF_fit.py v1 script. Figure 8 shows the calculated shift factors and the WLF fit over the temperature. Table 5 shows the fitted WLF parameters. The fitted function agrees well with the data points. Since the WLF equation is explicitly valid for the glass transition zone, we observe a higher deviation at the temperatures at the ends of the scale. It is important to note that on the logarithmic y-axis, the deviation may appear smaller than it actually is for higher shift factors.

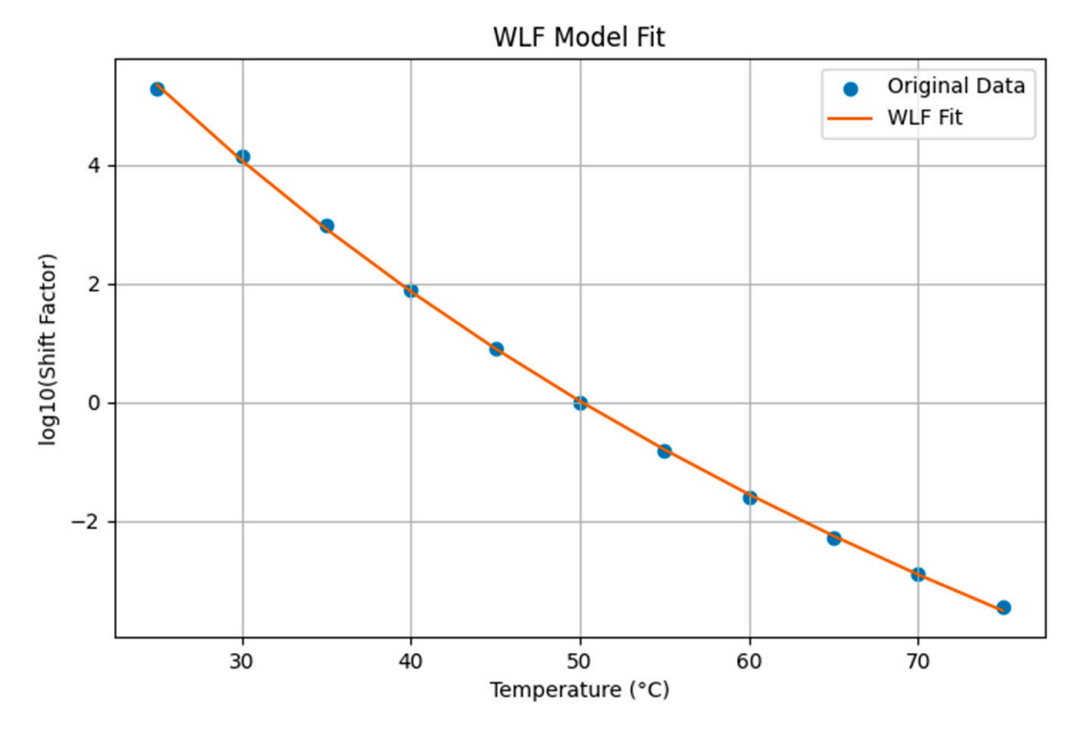


Figure 8. Plot of the WLF fit and the shift factors.

Table 5. WLF parameters and reference temperature.

Parameter	Value
$T_{ m ref}$	50 °C
C_1	48.134
C_2	123.139

The final step is to fit the complex modulus master curve using the Prony series from Equation (5). This is again performed using the curve_fit function from the Scipy 1.14.1 Python package. The script Prony_FrequencyDomain.py v1 reads the frequencies f_{shift}, as well as the storage and loss modulus from the master curve, and optimizes E_{∞} as well as a defined number of E_k and τ_k pairs. In this study, a number of ten pairs (k = 10) is chosen. The fitted parameters are shown in Table 6. Since ANSYS 2023R2 and ABAQUS 2024 require relative moduli ek as input data for the Prony series parameters, these values are calculated as described by Formulas 8 and 9. The master curve for the storage and loss modulus and its approximation by the Prony series, using the fitted parameters, are shown in Figure 9. The Prony series fit closely follows the experimental storage modulus data over the entire frequency range. This indicates that the Prony fit accurately captures the elastic response of the material at all frequencies. This means that the elastic behavior is well approximated on both short and long-time scales. It indicates an accurate prediction of the stiffness ratio. In the recovery phase, an accurate storage modulus fit indicates a good prediction of the shape recovery ratio. The Prony fit follows the experimental loss modulus master curve reasonably well between 10×10^{-3} and 10 Hz, underestimating the values by a small margin. Outside these values, the deviation increases significantly. Underestimating the loss modulus can lead to shorter relaxation times because it affects the rate of energy dissipation and relaxation during the recovery phase. As a result, the simulation may underpredict viscous drag and energy dissipation, resulting in a faster recovery.

$$E_0 = E_{\infty} + \sum_{k=1}^{n} E_k \tag{8}$$

$$e_k = E_k / E_0 \tag{9}$$

Table 6. Prony series parameters.

k	$E_{\mathbf{k}}$	e_k	$ au_{\mathbf{k}}$
0	1835.32		
1	142.31	0.0775392	3.5724×10^{-5}
2	128.83	0.07019229	2.8319×10^{1}
3	64.89	0.03535694	4.5035×10^{3}
4	106.54	0.05804762	1.6540×10^{-6}
5	196.74	0.107198	5.0093×10^{-4}
6	233.04	0.12697283	5.2998×10^{-2}
7	89.67	0.04885859	2.9857×10^{2}
8	200.00	0.10897322	3.9825×10^{-1}
9	242.63	0.13220081	5.8732×10^{-3}
10	166.10	0.09050048	3.0959
∞	264.58		

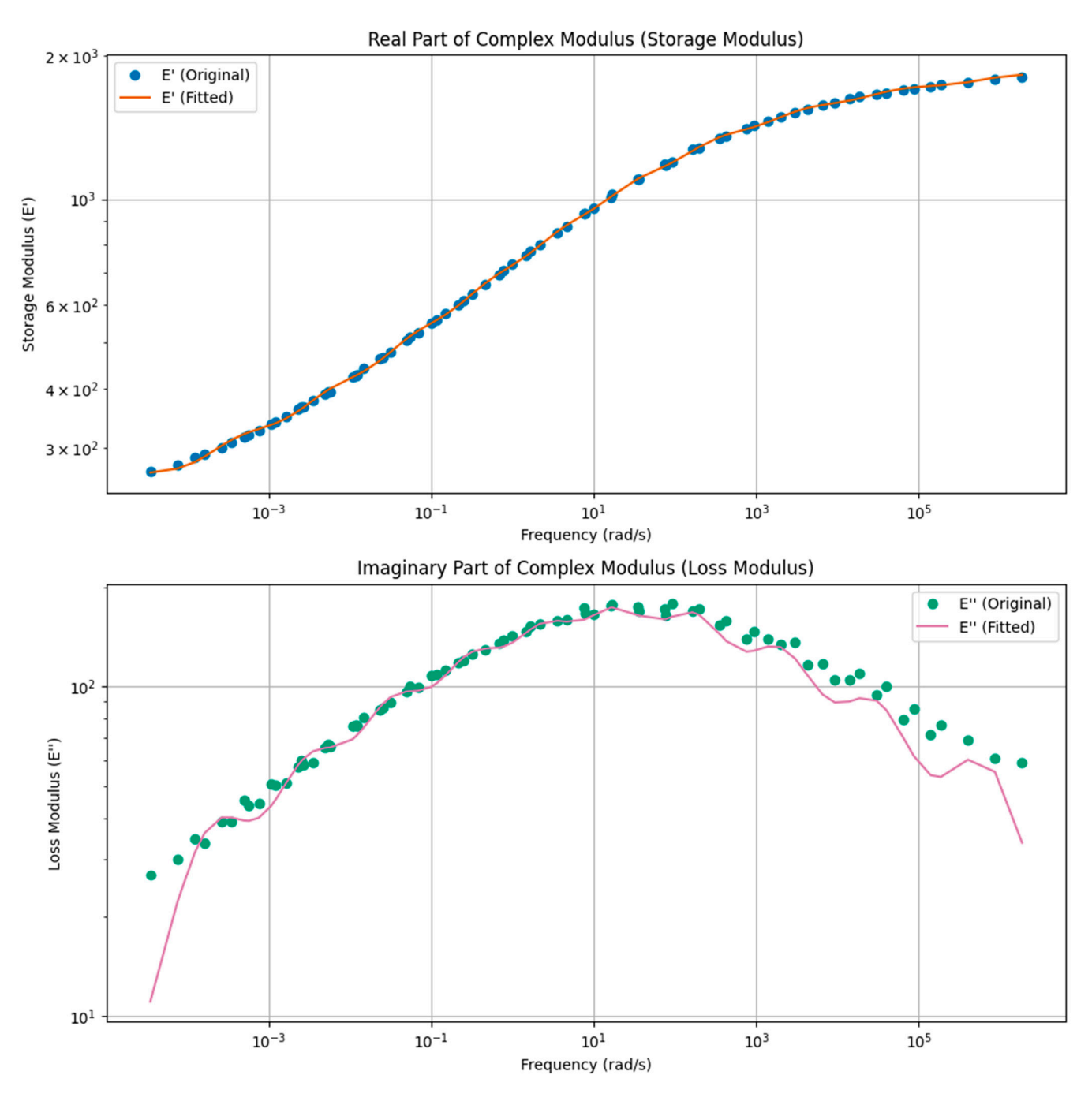


Figure 9. Master curves of the storage portion (**upper** plot) and loss portion (**lower** plot) of the complex tensile modulus and fitted curves using Python *Scipy curve_fit*.

3.4. Results of the Rheometer Shape-Memory Test

The shape memory test is performed using the Anton Paar MCR 702 rheometer with linear drive, as described in 2.7. Figure 10 shows the maximum deformation of the sample over time. The diagram shows the expected behavior. The first sample is stretched to 4.3% strain. During cooling, the strain decreases to 4.1%. This can be explained by the negative thermal expansion of the specimen fixture and the increasing internal stress within the specimen, causing the deformation of the fixture. The elastic strain is then released, reducing the strain to 3.2%, resulting in a shape fixity ratio of 74.4%. A small increase in the strain can be observed during the heating due to thermal expansion. This is followed by a reduction in the strain to 0.9%, after heating above the glass transition or shape memory activation temperature. The sample shows a shape memory effect, but retains some plastic

deformation, resulting in a shape recovery ratio of 79.1%. Sample two is stretched to a 4.66% strain. During cooling, a small loss in the strain is observable again. After a force release a shape fixity ratio of 79.7% is measured. Activated by heating, the sample shows a shape memory effect, but retains some plastic deformation, resulting in a shape recovery ratio of 76.6%.

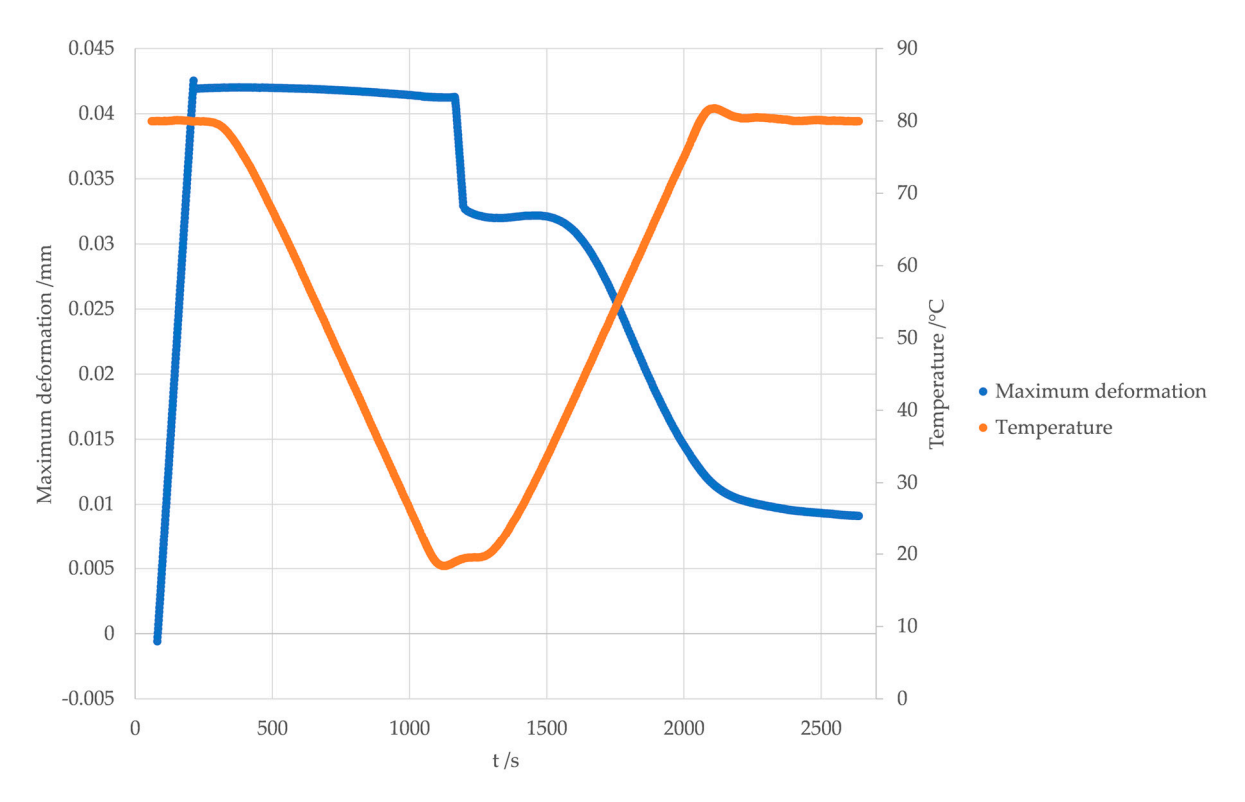


Figure 10. Results of the rheometer shape–memory test: maximum deformation and temperature over time for Test 1. Programming: t = 0-1100 s, Force Release: t = 1100-1150 s, Recovery: t = 1150-2600 s.

3.5. Implementation in ANSYS Mechanical

As mentioned earlier, the implementation follows the procedure established by Azzawi et al. [35]. With their publication, an easy-to-follow guideline for ABAQUS 2024 is already available. Since there is no guideline for ANSYS 2023R2 in the literature, this study transfers the mentioned procedure to the static structural analysis in Ansys Mechanical 2023R2. For a static structural analysis, the governing equation is the balance of linear momentum, simplified for a static case. Since thermal strains are included, the governing equation considers the changes in stress due to the temperature-dependent strain. For the constitutive relation, the Prony series and WLF parameters can be entered in the technical data under "Viscoelastic". The Prony series represents the time- and temperaturedependent stress relaxation, while the WLF parameters allow for an adjustment of the material behavior based on temperature changes. In addition, Poisson's ratio, coefficient of thermal expansion, and Young's modulus for isotropic elasticity and thermal expansion are added from the material data sheet [46]. Next, the geometry of the shape memory test specimen is modeled and added as geometry. The model is then meshed using SOLID186 elements. These 20-node brick elements offer quadratic shape functions, providing a high accuracy in nonlinear and thermal analyses. Each element is a cube of 0.2 mm side length. This results in a total of 2680 elements and 14,238 nodes. Each node in a SOLID186 element has three translational degrees of freedom. A temperature boundary condition, a fixed support (one face of the long side of the specimen), and a displacement boundary condition (opposite face of the long side of the specimen) are introduced. The analysis is set up in six steps. The step times are derived from the test data of the shape memory test to account

for the deviation from the test input times in the heating and cooling phases due to the heat capacity of the oven. The calculation is set to nonlinear, with thermal strain effects enabled. The program control Newton-Raphson method is used. The large deflection and quasi-isotropic solution settings are also turned on. All other parameters are listed in Table 7. The calculation follows the experimental scheme shown in Figure 2.

Time Step	0	1	2	3	4	5	6
Description	Initial	Heating	Cooling	Releasing	Holding	Heating	Holding
End time/s	0	152	1108	1147	1247	2026	2577
Sub-steps	0	10	10	10	10	50	10
Thermal condition/°C	80	80	20	20	20	80	20
Displacement/mm	0	0.43	0.43				

Table 7. Time steps and parameters for the ANSYS Mechanical simulation.

The simulation result is plotted with the test data and shown in Figure 11. During the loading phase, we observe a very good correlation between the test data and the simulation. During cooling, we see an increasing deviation between simulation and test data. The deformation in the experimental data decreases, possibly due to thermal expansion in the specimen holder, as already discussed in Section 3.4. When the clamping force is released, the simulation continues to closely match the test data. This is consistent with an accurate prediction of the deformation ratio. During the recovery phase, we see a noticeable deviation between the simulation and test data. The simulation predicts a faster recovery, followed by a gradual increase in deformation. Interestingly, the gradient of this last increase mimics the gradient of the increase in deformation just before the recovery under increasing temperature. This suggests a thermal expansion process. The experimental data show a slower and more steady decrease in deformation during the recovery phase. However, the recovery process starts at the same time in the test and the simulation, without a clear thermal expansion step. Finally, both the simulation and test data agree on the residual deformation after shape recovery. The key values of the shape memory cycles are summarized in Table 8.

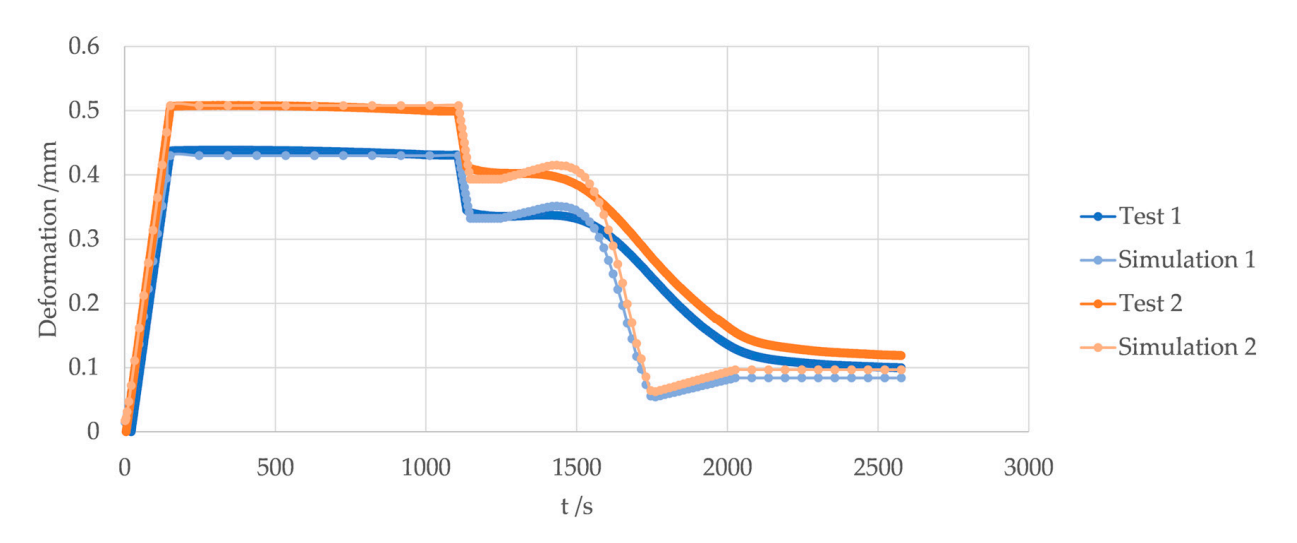


Figure 11. Comparison of the simulation and test data deformation over time. Programming: t = 0-1100 s. Force Release: t = 1100-1150 s. Recovery: t = 1150-2600 s.

Table 8. Comparison of key values from test data and simulation.

	Test 1/Simulation 1	Test 2/Simulation 2	Mean
Shape fixity ratio	76.9%/75.7%	79.7%/77.4%	78.3%/76.6%
Deviation	1.2%	2.3%	1.7%
Shape recovery ratio	77.2%/80.9%	76.6%/81.0%	76.9%/80.9%
Deviation	3.7%	4.4%	4.0%

4. Discussion

This study aims to provide guidelines from the material coupon tests, through their evaluation, to the implementation of the material model in FEA software for SMP, using fully open-source and transparent methods. The methods used are described in Section 2. All developed Python scripts used for parameter identification and curve fitting for the Master curve, WLF equation, and Prony series are open-source and accessible from Gitlab. The link can be found in the Supplementary Materials. The DSC results are within the expected range and are used to define the temperature range for the DMA test to measure the complex tensile modulus. Storage and loss moduli match well with the reviewed literature. Notably, the T_g measured by the DSC differs from the T_g measured by the DMA. This is why 55.8 °C was measured as T_g in Section 3.2, while 50 °C is used as the reference for setting up the master curve and the midpoint of the shape memory test. This discrepancy is expected due to the different measurement principles between the DSC and the DMA. The DSC measures the heat flow through the sample and T_g is associated with the step change in heat capacity. This value depends on the heating rate. Standard ISO or ASTM DSC methods, such as the one used in this study, recommend heating and cooling rates of 10 K per minute. This value is higher than the rates used in shape memory testing or in a DMA. The slower heating rate allows more time for molecular relaxation, resulting in a lower $T_{\rm g}$. However, $T_{\rm g}$ measured by DMA is frequency dependent. Higher frequencies result in a higher T_g , while at lower frequencies the material has more time to exhibit relaxation behavior in response to the applied stress, resulting in a lower measured T_g . The storage and loss modulus data obtained are within the expected range and show the expected behavior over temperature (Figure 6) and frequency (Figure 7a). Furthermore, the master curve constructed in Figure 7b is a smooth curve, indicating high-quality measurement data and a proper working shift in the data series using the Mastercurves 0.2.3 Python package in mastercurve.py v1. The curve fit for the WLF equation shows an agreement with the applied shift factors, as shown in Figure 8. This indicates that the WLF parameters are correct and that the WLF_fit.py v1 script is working properly. As shown in Figure 9, the Prony series curve fit agrees with the storage modulus master curve. For the loss modulus master curve, the curve fit shows very good coherence around the glass transition, with increasing deviation at higher and lower frequencies. Since the Prony series is used to model the behavior of the material around its glass transition, this can be accepted. This validates the derived Prony parameters and the Prony_FrequencyDomain.py v1 script. The shape memory test shows good results, as shown in Figure 10. However, the elastic recovery after releasing the displacement is quite high. Therefore, the PA6 used shows a shape fixity rate of only 74%, which is very low, compared to published shape memory polymer formulations that allow a shape fixity rate of over 99% [51]. Furthermore, the measured shape recovery rate is 79%. This is also low compared to other shape memory polymers [51]. However, PA6 was not primarily chosen for its shape memory capabilities, but for its properties for disposable mandrels in composite manufacturing. Therefore, shape memory capabilities were important, but the exact performance was of secondary interest in the material selection. This does not limit the applicability of the methods

described in this work to other shape memory polymers. Another very important issue is the degradation of the shape memory properties of the thermoplastic polymers after recycling. Since this study aims to provide a material-to-solution framework, from material testing to the simulation of shape memory behavior, material degradation is not addressed in this study. In order to investigate shape fixation and shape recovery for multiple recycling steps, the provided workflow can be easily used to ensure reproducibility in each described part of the workflow. Follow-up research will provide deeper insight into this topic, with respect to the material investigated in this study. The DSC, DMA, and the described shape memory test can be easily performed with other polymers by changing the respective test parameters to the values valid for the chosen polymer. How to find these parameters is described in the test standards or in the methods section of this paper. All Python scripts used in this work are applicable to test data derived from other polymer materials, using the described methods. A description of how to adapt these scripts to the respective parameters is provided in the header of the scripts.

The DSC and DMA are widely used thermal and mechanical analysis techniques. Major errors in a DSC include the following: instrument errors, such as inaccurate calibration of temperature and heat flow; sample preparation errors, such as contamination, mismeasured mass, or pan contact errors; environmental errors, such as ambient temperature fluctuations or shocks; and operational errors, such as incorrect test programs or misinterpretation of results. To address these potential errors, we used a calibrated Mettler DSC 2 TOPEM to check the samples for contamination and the pans for buckling or dents that indicate poor contact. All measurements were carried out in the controlled environment of the thermal analysis laboratory at the DLR Institute of Lightweight Structures in Braunschweig, Germany. Operating errors have been addressed by following the DSC standard DIN EN ISO 11357 [52]. All results were derived and evaluated separately by the authors to avoid misinterpretation. The main errors in a DMA are as follows: instrumental errors, such as sample, clamp, or fixture misalignment; sample preparation errors, such as inconsistent geometry or defects and internal stresses; environmental errors, such as humidity or temperature variations; and operational errors, such as incorrect frequencies or strain amplitudes. Our specimens were produced with precision-milled injection molds and measured multiple times with calibrated measuring tools. All specimens were dried and annealed to relieve internal stresses and eliminate moisture. The controlled environment of the test lab minimizes environmental errors. The DMA test setup was iterative to achieve the correct frequency and strain amplitude for the material used. The shape memory test setup was developed iteratively. This allowed us to eliminate potential errors step-by-step and ensure a valid test procedure. The DMA and shape memory tests were performed in a calibrated, high-precision Anton Paar MCR 702 rheometer. This ensures full reproducibility of our experiments with the parameters discussed in this study. Implementing viscoelastic material properties and setting up the shape memory cycle in ANSYS 2023R2 Mechanical is straightforward. The simulation correlates with the test data until the displacement is released, as shown in Figure 11. A smaller discrepancy during the first cooling phase can be explained by the increasing stress due to the negative thermal expansion of the specimen and the fixture. After the release, the simulated thermal expansion is higher than the measured one. This can be explained by a possible deviation between the real thermal expansion coefficient of the sample and the one derived from the data sheet and used for the simulation. However, the activation temperature for the shape memory effect is the same in simulation and test, since both data series start the shape recovery at the same time. The simulation then shows a much higher recovery rate than the test data. This could be due to the small tensile force applied to the specimen by the fixture during shape recovery, and the delay due to the thermal capacity of the specimen and the oven. A more reasonable

explanation for the mismatch during the recovery phase is the underestimation of the loss modulus by the Prony series, as shown in Figure 9. Since the loss modulus accounts for energy dissipation and relaxation behavior during recovery, an underestimate results in a less viscous resistance. This results in a faster predicted recovery and the simulation fails to reproduce the gradual energy dissipation observed in the experimental data. To simplify the curve fitting process and avoid convergence problems, the Prony series in the Python script used only fits the parameters to the loss modulus test data, while simply applying these parameters to the loss modulus data. We modified the code provided in this study to fit the parameters to both experimental data sets, memory, and loss modulus, at the same time, but continued to run into convergence problems and less accurate curve fits than in the proposed way. More advanced curve fitting packages such as the standard curve_fit function in Python Scipy 1.14.1 package could potentially overcome these problems. However, both the simulation and test reach the recovered shape at the same time with the same shape recovery rate. This indicates that the applied methods are capable of accurately predicting the shape fixation ratio, the shape recovery ratio, and the start and end points of the recovery process. These are critical considerations in the accurate design of single use disposable shape memory polymer mandrels for hollow composite profile manufacturing. In this scenario, the actual behavior of the mandrel between the temporary and recovered shape is less important than the accurate prediction of these states and the time for shape recovery. Overall, the methods described in this study meet the requirements of the overarching scenario. The methods are transferable to other polymers and provide an open-source guide from the material testing and parameter identification to the implementation in proprietary finite element software such as ANSYS 2023R2 or ABAQUS 2024. The following implementation guidelines should help to reproduce our results:

- 1. FEA Software Setup
 - ANSYS Mechanical 2023.2
 - Package: Static Structural
 - Governing equation: Linear momentum balance for static case
- 2. Material Data Setup
 - Material data sheet: Poisson's Ratio, Elastic Modulus, Coefficient of thermal expansion
 - DMA test data: Prony parameters, WLF parameters
- 3. Geometry and Meshing
 - Test specimen modeled in 3D
 - Mesh-elements: SOLID186 (20-node brick, quadratic shape function)
 - Mesh-size: 0.2 mm
- 4. Boundary conditions
 - Temperature
 - Fixed support (one face)
 - Displacement (opposite face)
- 5. Analysis setup
 - Six steps (step total times derived from test data)
 - Nonlinear analysis (Newton-Raphson program controlled)
 - Large deflection
 - Quasi-isotropic solution
 - Refer to Table 7 for detailed parameters

Figure 12 shows a schematic summary of the "material-to-solution" approach developed in this study.

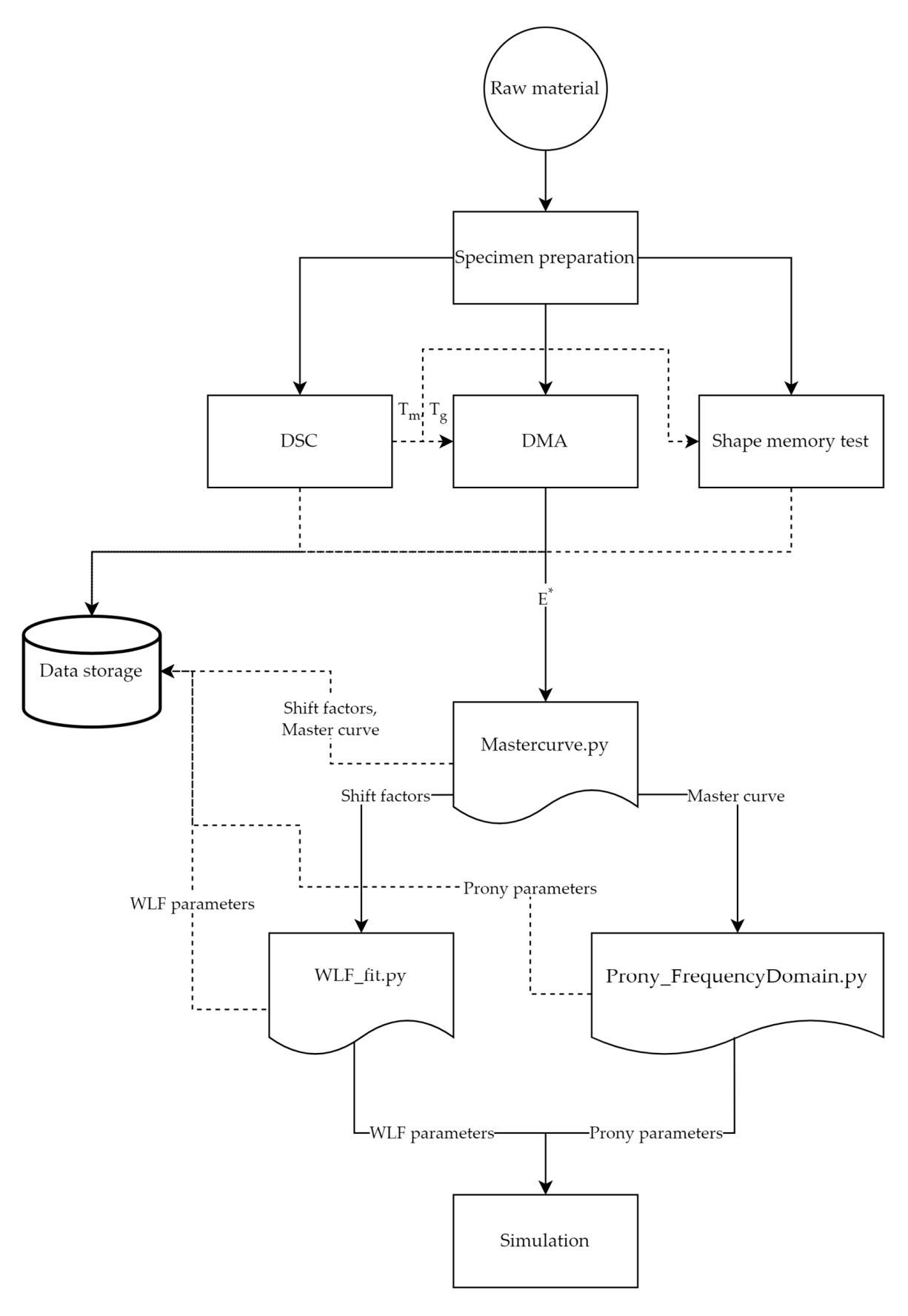


Figure 12. Schematic summary of the "material-to-solution" approach derived in this work.

When comparing the results of our study with the related literature, it is important to understand the differences in methodology. Yu et al. [42] and Azzawi et al. [35] used stress

relaxation tests to derive their master curve and calculate the Prony parameters. Frequency sweeps, as proposed in this paper, were used by Diani et al. [33]. Frequency sweeps are a more practical and time-efficient method for constructing master curves when a dynamic mechanical analyzer is available. The properties of SMPs with moderate to fast relaxation times can be more accurately captured. The derived data are in the frequency domain, and the Prony fit is more complex as storage and loss modulus curves must be fitted for best results. Stress relaxation tests are better suited for slow relaxation time systems. However, the experimental setup is less complex, and the derived data are in the time domain, where it is easier to fit the Prony series to a single curve. The study by Azzawi et al. [35] shows very good agreement between their master curve from relaxation tests and the Prony fit in the time domain. It is noteworthy that only five Prony terms were used to derive their material model. They study the shape memory effect of a bent beam. The simulation accurately predicts the shape fixity ratio, but shows some discrepancy in the shape recovery step. While our study overestimates the shape recovery gradient, Azzawi et al. underestimate it. The shape recovery ratio is not evaluated. Yu et al. [42] used twelve Prony terms to fit the master curve from the stress relaxation test. However, their fitted function shows alternating discrepancies with the experimental data over the entire time scale. Their model overestimates the shape fixity and shape recovery ratios, as well as the shape recovery time. Diani et al. [33] also used twelve terms to calculate their Prony fit from the DMA test data in the frequency domain. Instead of plotting storage and loss modulus plots, they plot storage modulus and $tan(\delta)$ plots. However, their Prony fit shows very good agreement with the storage modulus experimental data, while the fitted curve underestimates the peak of the $tan(\delta)$, which correlates with an underestimation of the loss modulus, resulting in a higher recovery gradient and faster recovery times in the simulation, compared to their experimental data. All of the discussed related literature shows the same drawbacks as our study. An underestimation of the storage modulus leading to a higher gradient in shape recovery. As discussed in the introduction, the Maxwell-Wiechert or Generalized Maxwell model is one of the simplest possible approaches to model the behavior of shape memory polymers. However, the prediction of the shape fixity ratio, the shape recovery ratio, and the start and end points of recovery in temperature and time can be simulated to a sufficient degree. For use in cases where the exact shape during the recovery phase is less important, this approach is a simple and efficient way to predict the overall behavior of shape memory polymers.

As described in the introduction, the overall research objective was to facilitate blowmolded thermoplastic shape-memory mandrels for the high-rate production of hollow fiber composite profiles. As our previous research has shown, PA6 and PET are promising materials for such mandrels [30]. The material-to-solution approach proposed in this study makes it possible to predict the key properties, shape fixation ratio, and shape recovery ratio of shape memory polymers in a straightforward, accessible, and reproducible manner. Future research will focus on the characterization of other thermoplastic materials, particularly PET, the transfer of the derived simulation approach from the coupon level to mandrel geometries, and the fabrication of blow-molded mandrels for simulation verification at this level. Subsequent research will focus on the manufacturing process of the hollow fiber profiles, in particular the winding or fiber placement process on blow-molded mandrels, the demolding process, and quality assurance. The results achieved will help manufacturers to quickly and economically design shape-memory thermoplastic mandrels and the tooling for their production. The necessary software tools, such as CAD, standard FEA programs, and integrated development environments, are widely used in the industry and do not require extensive additional programming of subroutines or the like. Subsequently, this will

enable a flexible, high-rate production of hollow fiber composite profiles, such as pressure vessels without liners, air intakes, or similar components.

5. Conclusions

The aim of this study was to provide the first guideline that spans from material coupon testing, through evaluation, to the implementation of the material model in FEA software for SMP using fully open source and transparent methods. PA6 was used as the material, but all methods are easily transferable to any other polymer material. We discussed the necessary thermo-rheological material tests, DSC and DMA, to derive the data and identify the parameters needed to implement the rheological generalized Maxwell model in proprietary FEA software such as ANSYS 2023R2 or ABAQUS 2024. For this purpose, we developed open-source Python scripts to fit these parameters. The software is available via the open repository Zenodo [45]. Furthermore, we introduced a tensile shape memory test using a rheometer with a linear drive. The simulation and the test agree in shape fixity ratio, shape recovery ratio, activation temperature, and recovery time. However, the explicit behavior of the specimen between the activation and full recovery showed some discrepancy between the simulation and test data. All the methods provided in this study are easily transferable to other polymer materials.

Supplementary Materials: The following supporting information can be downloaded at: https://www.mdpi.com/article/10.3390/jmmp9030073/s1. All Python scripts for parameter identification and curve fitting mentioned in this study are publicly available online at: https://doi.org/10.5281/zenodo.14330773 (accessed on 9 December 2024).

Author Contributions: Conceptualization, F.N.; methodology, F.N. and F.C.; software, F.N.; validation, F.N. and F.C.; formal analysis, F.N. and F.C.; investigation, F.N. and F.C.; data curation, F.N.; writing—original draft preparation, F.N.; writing—review and editing, F.N., F.C. and M.S.; visualization, F.N. All authors have read and agreed to the published version of the manuscript.

Funding: The research was carried out within the framework of the German Aerospace Center's core funded research. The research received funding from the German Research Foundation (DFG)—Project-ID: 447858794.

Institutional Review Board Statement: Not applicable.

Data Availability Statement: The original contributions presented in this study are included in the Supplementary Materials. Further inquiries can be directed to the corresponding author(s).

Acknowledgments: Special thanks to Monika von Monkiewitsch, head of the thermal analysis laboratory at the DLR—Institute of Lightweight Systems in Braunschweig, for her supervision and help during the thermal analysis tests. Thanks to José Alberto Rodríguez Agudo, Lead Scientist at Anton Paar, for the support in operating the MCR 702. DeepL Write was used in this work for spell checking and language editing purposes to ensure and enhance readability and understanding. All output was critically reviewed, treated as a recommendation, and revised where necessary prior to implementation.

Conflicts of Interest: The authors declare no conflicts of interest. The funders had no role in the design of the study; in the collection, analyses, or interpretation of data; in the writing of the manuscript; or in the decision to publish the results.

Abbreviations

The following abbreviations are used in this manuscript:

AFP Automated Fiber Placement DLR German Aerospace Center **DMA** Dynamic Mechanical Analysis DSC Differential Scanning Calorimetry **FEA** Finite element analysis **FRP** Fiber-reinforced Polymer **GMM** Generalized Maxwell Model **MCR** Modular Compact Rheometer **RTM** Resin Transfer Molding **SME** Shape Memory Effect **SMP** Shape Memory Polymer SRF Solid Rectangular Fixture TTS Time-Temperature Superposition UAV Unmanned Aerial Vehicle **UMAT** User-defined Mechanical Material Behavior WLF Williams-Landel-Ferry

References

- 1. Li, Y.; Xiao, Y.; Yu, L.; Ji, K.; Li, D. A review on the tooling technologies for composites manufacturing of aerospace structures: Materials, structures and processes. *Compos. Part A Appl. Sci. Manuf.* **2022**, 154, 106762. [CrossRef]
- 2. Hader, M.; Baur, S.; Kopera, S.; Schönberg, T.; Hasenberg, J.-P. Urban Air Mobility. 2020. Available online: https://www.rolandberger.com/publications/publication_pdf/roland_berger_urban_air_mobility_1.pdf (accessed on 23 October 2023).
- 3. Xiang, S.; Xie, A.; Ye, M.; Yan, X.; Han, X.; Niu, H.; Li, Q.; Huang, H. Autonomous eVTOL: A summary of researches and challenges. *Green Energy Intell. Transp.* **2024**, *3*, 100140. [CrossRef]
- 4. Pierrejean, E. JEC Observer: Overview of the global composites market 2022–2027. 2023. Available online: https://www.jeccomposites.com/wp-content/uploads/2023/06/v2_14985_DP-UK_JEC-Observer-ECO.pdf (accessed on 22 February 2023).
- 5. Strong, A.B. Fundamentals of Composites Manufacturing, 2nd ed.; Society of Manufacturing Engineers: Dearborn, MI, USA, 2008.
- 6. Lehmann, U.; Michaeli, W. Cores lead to an automated production of hollow composite parts in resin transfer moulding. *Compos. Part A Appl. Sci. Manuf.* **1998**, 29, 803–810. [CrossRef]
- 7. Neumann, F. Variable Shape Tooling for Composite Manufacturing: A Systematic Review. J. Compos. Sci. 2024, 8, 131. [CrossRef]
- 8. Makki, T.; Vattathurvalappil, S.H.; Theravalappil, R.; Nazir, A.; Alhajeri, A.; Azeem, M.A.; Mahdi, E.; Ummer, A.C.; Ali, U. 3D and 4D printing: A review of virgin polymers used in fused deposition modeling. *Compos. Part C Open Access* **2024**, *14*, 100472. [CrossRef]
- 9. Du, H.; Liu, L.; Zhang, F.; Zhao, W.; Leng, J.; Liu, Y. Thermal-mechanical behavior of styrene-based shape memory polymer tubes. *Polym. Test.* **2017**, *57*, 119–125. [CrossRef]
- 10. Everhart, M.C.; Stahl, J. Reusable shape memory polymer mandrels. Proc. SPIE 2005, 5762, 27–34. [CrossRef]
- 11. Lu, X.; Jing, X.; Zou, J.; Zhang, C.; Wu, C.; Chen, S. A thermoplastic resin matrix and its physical properties suitable for deformable mandrel. *J. Phys. Conf. Ser.* **2021**, 2083, 022080. [CrossRef]
- 12. Yan, C.; Li, G. Tutorial: Thermomechanical constitutive modeling of shape memory polymers. *J. Appl. Phys.* **2022**, *131*, 111101. [CrossRef]
- 13. Xiao, X.; Kong, D.; Qiu, X.; Zhang, W.; Liu, Y.; Zhang, S.; Zhang, F.; Hu, Y.; Leng, J. Shape memory polymers with high and low temperature resistant properties. *Sci. Rep.* **2015**, *5*, 14137. [CrossRef] [PubMed]
- 14. Xiao, X.; Kong, D.; Qiu, X.; Zhang, W.; Zhang, F.; Liu, L.; Liu, Y.; Zhang, S.; Hu, Y.; Leng, J. Shape-Memory Polymers with Adjustable High Glass Transition Temperatures. *Macromolecules* **2015**, *48*, 3582–3589. [CrossRef]
- 15. Cho, J.W.; Kim, J.W.; Jung, Y.C.; Goo, N.S. Electroactive Shape-Memory Polyurethane Composites Incorporating Carbon Nanotubes. *Macromol. Rapid Commun.* **2005**, *26*, 412–416. [CrossRef]
- 16. Kim, B.K.; Lee, J.S.; Lee, Y.M.; Shin, J.H.; Park, S.H. Shape memory behavior of amorphous polyurethanes. *J. Macromol. Sci. Part B* **2001**, *40*, 1179–1191. [CrossRef]
- 17. Beblo, R.; Gross, K.; Weiland, L.M. Mechanical and Curing Properties of a Styrene-based Shape Memory Polymer. *J. Intell. Mater. Syst. Struct.* **2010**, *21*, 677–683. [CrossRef]
- 18. Zhang, D.; Liu, Y.; Yu, K.; Leng, J. Influence of cross-linking agent on thermomechanical properties and shape memory effect of styrene shape memory polymer. *J. Intell. Mater. Syst. Struct.* **2011**, 22, 2147–2154. [CrossRef]
- 19. Leng, J.; Wu, X.; Liu, Y. Effect of a linear monomer on the thermomechanical properties of epoxy shape-memory polymer. *Smart Mater. Struct.* **2009**, *18*, 095031. [CrossRef]

- 20. Leng, J.; Xie, F.; Wu, X.; Liu, Y. Effect of the γ-radiation on the properties of epoxy-based shape memory polymers. *J. Intell. Mater. Syst. Struct.* **2013**, 25, 1256–1263. [CrossRef]
- 21. Biju, R.; Gouri, C.; Nair, C.R. Shape memory polymers based on cyanate ester-epoxy-poly (tetramethyleneoxide) co-reacted system. *Eur. Polym. J.* **2012**, *48*, 499–511. [CrossRef]
- 22. Xie, F.; Huang, L.; Liu, Y.; Leng, J. Synthesis and characterization of high temperature cyanate-based shape memory polymers with functional polybutadiene/acrylonitrile. *Polymer* **2014**, *55*, 5873–5879. [CrossRef]
- 23. Wang, K.; Zhu, G.; Wang, Y.; Ren, F. Thermal and shape memory properties of cyanate/polybutadiene epoxy/polysebacic polyanhydride copolymer. *J. Appl. Polym. Sci.* **2015**, *132*, 42045. [CrossRef]
- 24. Liu, Y.; Lv, H.; Lan, X.; Leng, J.; Du, S. Review of electro-active shape-memory polymer composite. *Compos. Sci. Technol.* **2009**, *69*, 2064–2068. [CrossRef]
- 25. Jiang, H.Y.; Kelch, S.; Lendlein, A. Polymers Move in Response to Light. Adv. Mater. 2006, 18, 1471–1475. [CrossRef]
- 26. Zhang, F.; Zhou, T.; Liu, Y.; Leng, J. Microwave synthesis and actuation of shape memory polycaprolactone foams with high speed. *Sci. Rep.* **2015**, *5*, 11152. [CrossRef] [PubMed]
- 27. Zhang, F.H.; Zhang, Z.C.; Luo, C.J.; Lin, I.-T.; Liu, Y.; Leng, J.; Smoukov, S.K. Remote, fast actuation of programmable multiple shape memory composites by magnetic fields. *J. Mater. Chem. C* **2015**, *3*, 11290–11293. [CrossRef]
- 28. Huang, W.M.; Yang, B.; An, L.; Li, C.; Chan, Y.S. Water-driven programmable polyurethane shape memory polymer: Demonstration and mechanism. *Appl. Phys. Lett.* **2005**, *86*, 114105. [CrossRef]
- Miadowitz, T. Beitrag zur Entwicklung blasgeformter Kernstrukturen für die Fertigung von CFK-Hohlprofilen. Dissertation, Technischen Universität Dresden, Dresden, Germany, 2019.
- 30. Neumann, F.; Rings, B.; Golombek, H.L. Investigation of thermoplastic polymers with regard to their suitability as mold material in the FRP manufacturing process. In Proceedings of the DLRK, Stuttgart, Germany, 19–21 September 2023.
- 31. Tobushi, H.; Hashimoto, T.; Hayashi, S.; Yamada, E. Thermomechanical Constitutive Modeling in Shape Memory Polymer of Polyurethane Series. *J. Intell. Mater. Syst. Struct.* **1997**, *8*, 711–718. [CrossRef]
- 32. Zhao, W.; Liu, L.; Lan, X.; Leng, J.; Liu, Y. Thermomechanical Constitutive Models of Shape Memory Polymers and Their Composites. *Appl. Mech. Rev.* **2022**, *75*, 020802. [CrossRef]
- 33. Diani, J.; Gilormini, P.; Frédy, C.; Rousseau, I. Predicting thermal shape memory of crosslinked polymer networks from linear viscoelasticity. *Int. J. Solids Struct.* **2012**, *49*, 793–799. [CrossRef]
- Simo, J. On a fully three-dimensional finite-strain viscoelastic damage model: Formulation and computational aspects. Comput. Methods Appl. Mech. Eng. 1987, 60, 153–173. [CrossRef]
- 35. Al Azzawi, W.; Epaarachchi, J.A.; Islam, M.; Leng, J. Implementation of a finite element analysis procedure for structural analysis of shape memory behaviour of fibre reinforced shape memory polymer composites. *Smart Mater. Struct.* **2017**, *26*, 125002. [CrossRef]
- 36. Liu, Y.; Gall, K.; Dunn, M.L.; Greenberg, A.R.; Diani, J. Thermomechanics of shape memory polymers: Uniaxial experiments and constitutive modeling. *Int. J. Plast.* **2006**, 22, 279–313. [CrossRef]
- 37. Chen, Y.-C.; Lagoudas, D.C. A constitutive theory for shape memory polymers. Part I. J. Mech. Phys. Solids 2008, 56, 1752–1765. [CrossRef]
- 38. Wang, Z.D.; Li, D.F.; Xiong, Z.Y.; Chang, R.N. Modeling thermomechanical behaviors of shape memory polymer. *J. Appl. Polym. Sci.* **2009**, *113*, 651–656. [CrossRef]
- 39. Baghani, M.; Naghdabadi, R.; Arghavani, J.; Sohrabpour, S. A constitutive model for shape memory polymers with application to torsion of prismatic bars. *J. Intell. Mater. Syst. Struct.* **2012**, 23, 107–116. [CrossRef]
- 40. Li, Y.; Hu, J.; Liu, Z. A constitutive model of shape memory polymers based on glass transition and the concept of frozen strain release rate. *Int. J. Solids Struct.* **2017**, *124*, 252–263. [CrossRef]
- 41. Qi, H.J.; Nguyen, T.D.; Castro, F.; Yakacki, C.M.; Shandas, R. Finite deformation thermo-mechanical behavior of thermally induced shape memory polymers. *J. Mech. Phys. Solids* **2008**, *56*, 1730–1751. [CrossRef]
- 42. Yu, K.; McClung, A.J.W.; Tandon, G.P.; Baur, J.W.; Qi, H.J. A thermomechanical constitutive model for an epoxy based shape memory polymer and its parameter identifications. *Mech. Time Depend. Mater.* **2014**, *18*, 453–474. [CrossRef]
- 43. Xin, X.; Lin, C.; Li, B.; Zeng, C.; Liu, L.; Liu, Y.; Leng, J. Self-driven intelligent curved hinge based on shape-morphing composites. *Compos. Struct.* **2024**, 345, 118329. [CrossRef]
- 44. Ji, J.; Zhang, K.; Guo, X. Shape memory polymer lattice structures with programmable thermal recovery time. *Smart Mater. Struct.* **2024**, *33*, 085027. [CrossRef]
- 45. Neumann, F. DMA-MaWProFit: Identify WLF-Equation and Prony Series Parameters from Frequency Domain DMA Test Data for Visco-Elastic Materials; Zenodo: Genève, Switzerland, 2024. [CrossRef]
- 46. Envalior Performance Materials LLC. Datasheet Durethan BC550Z 900116 DUSXBL 2023. Available online: https://techcenter.lanxess.com/scp/americas/en/products/datasheet/LANXESS_Durethan_BC550Z_900116_DUSXBL_ISO_EN.pdf?docId=31484752 (accessed on 10 February 2025).

- 47. Tschoegl, N.W. The Phenomenological Theory of Linear Viscoelastic Behavior; Springer: Berlin/Heidelberg, Germany, 1989.
- 48. Lennon, K.R.; McKinley, G.H.; Swan, J.W. A Data-Driven Method for Automated Data Superposition with Applications in Soft Matter Science. 2022. Available online: http://arxiv.org/pdf/2204.09521 (accessed on 10 February 2025).
- Lennon, K.R.; Swan, J.W. Automatic Identification of Similarity Relations from Data; Massachusetts Institute of Technology: Cambridge, MA, USA, 2023; Available online: https://github.com/krlennon/mastercurves (accessed on 10 February 2025).
- 50. Williams, M.L.; Landel, R.F.; Ferry, J.D. The Temperature Dependence of Relaxation Mechanisms in Amorphous Polymers and Other Glass-forming Liquids. *J. Am. Chem. Soc.* **1955**, 77, 3701–3707. [CrossRef]
- 51. Zhao, W.; Li, N.; Liu, L.; Leng, J.; Liu, Y. Mechanical behaviors and applications of shape memory polymer and its composites. *Appl. Phys. Rev.* **2023**, *10*, 011306. [CrossRef]
- 52. DIN EN ISO 11357-1:2023-06; Kunststoffe_-Dynamische Differenzkalorimetrie_(DSC)_-Teil_1: Allgemeine Grundlagen (ISO_11357-1:2023); Deutsche Fassung EN_ISO_11357-1:2023. International Organization for Standardization: Geneva, Switzerland, 2023. [CrossRef]

Disclaimer/Publisher's Note: The statements, opinions and data contained in all publications are solely those of the individual author(s) and contributor(s) and not of MDPI and/or the editor(s). MDPI and/or the editor(s) disclaim responsibility for any injury to people or property resulting from any ideas, methods, instructions or products referred to in the content.